Theoretical design of an Integrated Optical Sensor for a Standard Immunoassay

Chen Chen, Xun Hou, and Jinhai Si*

Abstract—Immunoassay is a biochemical test that measures the presence or concentration of biomolecule in a solution by the means of the antibody (or antigen). Most immunoassays involve chemically linking antibodies or antigens with some kind of detectable labels which produce measurable signals in response to the binding. The use of labels create problems including complexity in the screening process and probable influence on the nature of target molecular. To overcome the drawbacks, we theoretically demonstrate an integrated Mach-Zehnder Interferometer (MZI) with n-shaped slot waveguide based on finite-element method. Dual polarization can be strongly confined in the slot where the analytes are accommodated. The interaction between the optical field and tested solution is greatly enhanced, resulting in high sensitivity of the device. The detection of surface adsorbed molecule densities is down to 0.176pg/mm² for transverse electric (TE) mode and 1.27pg/mm² for transverse magnetic (TM) mode. The integrated MZI with identical configuration of both arms make the parallel-control trial available thereby effectively preventing the unspecific binding and background from biological materials. Wavelength interrogation was taken to monitor the antibody-antigen recognition.

Index Terms—Integrated Optics, immunoassay, parallel-control trial, finite-element-method.

I. INTRODUCTION

An immunoassay relies on the ability of an antibody to recognize and bind the corresponding antigen and thus measure the presence or concentration of an analyte. One component of an immunoassay is the antibodies that have been selected carefully to ensure the analyte being detected at low concentration and with high specificity. Another key feature is a means to produce a measurable signal in response to the binding. Various labels, such as enzymes, radioactive isotopes and fluorogenic reporters are introduced and allow for detection by different means[1-3]. All labels, without exception, are chemically linking or conjugated to the desired antibody (or antigen) and thus bring about complexity in the screening process and probable influence on the nature of target molecular. In this context, the demand for label-free

This work is initially submitted for review on Feb.9th 2018. This work was supported by the National Natural Science Foundation of China (NSFC) under Grant Nos. 61235003 and 61427816.

Chen Chen, Xun Hou and Jinhai Si are with the Key Laboratory for Physical Electronics and Devices of the Ministry of Education and Shaanxi Key Lab of Information Photonic Technique, School of Electronics and Information Engineering, Xi'an Jiaotong University. (e-mail: xjtuchenchen@stu.xjtu.edu.cn, houxun@opt.ac.cn, jinhaisi@mail.xjtu.edu.cn).

biochemical technologies is coming. The label-free integrated optical biosensors have been heavily exploited in biochemical among which evanescent wave techniques[4-10] present good performance on the detection. Mechanism of most label-free biosensors is based on evanescent field sensing. Within the evanescent field, analytes recognize with partner receptors already immobilized onto the surface of waveguide and thus affecting the guiding properties of waveguide, concretely, shifts in effective mode index. The most common evanescent wave device is surface plasmon resonance (SPR) techniques[11-14]. Though SPR biosensor has been widely investigated and hundreds of publications have demonstrated its outstanding performance to evaluate complex biosensing interactions, the intrinsic size and difficulty in miniaturization set limits on its development and application. Photonic sensors based on integrated optics (IO) with high potential for chip integration can solve the aforementioned SPR problems. IO devices have attractive attributes[15] such as ultra-high sensitivity, response time, miniature dimension, multi-analyte detection and protection against external interference. Among various IO sensors, integrated Mach-Zehnder Interferometer (MZI)[4-7] is the most promising for biosensing in virtue of their high sensitivity and broad dynamic range. The MZI architecture[14] is consist of two parallel channels-the sensing arm and the reference arm, by means of two Y-junctions. When it is employed for biosensing, biomolecular interactions which take place in the sensing arm could be probed by the evanescent field. The extra strength is that the reference arm makes the parallel-control trial done easily and thus preventing unspecific binding and external disturbance. Since a carefully designed parallel-control trial, to great extent, determines the reliability of a biochemical result. Recently, we have reported an optical biosensor[10] for characterizing protein conformational change. A design of parallel-control trial is not required for the extraction of surface mass density of desired protein in that case. For an immunoassay, however, a biosensor with ability of taking control trail is necessary and important. Herein, the demonstrated integrated optics is designed to carry on a control trail. Normally, effective mode index change is ultimately converted to an intensity modulation in the output of MZI. The noise from laser or light source intensity fluctuations and thermal variations can strongly affect the value of output intensity. As an alternative, we take wavelength interrogation to interpret the effective index change so that more reliable result can be achieved. Thus, the demonstrated device is from the improving of the previous one.

Grating coupled waveguide sensors are one of the first sensors earlier investigated. A grating coupler with periodic disturbance in a planar waveguide, allows to excite a guided

mode at certain angle of incident light when the incoupling condition satisfied. A variety of configurations have been demonstrated, amongst which the most attractive ones are grating coupled interferometry (GCI) and resonance waveguide grating (RWG). GCI, a simple and cost-effective device, was commercially developed for multichannel biosensing [16,17]. It smartly combines grating coupled waveguides with the interferometric measurements. In the latest report[18], the sensing length (5mm long area between two incoupling gratings) can be greatly increased and precisely controlled by introducing two incoupling and one outcoupling grating areas to the planar optical waveguide. Instead of two separated and parallel beams that most interferometric arrangements adopted, a single expanded beam illuminating both incoupling gratings simultaneously. A two-cell liquid crystal modulator is located in the path of the beam. In this way, half of the beam is phase modulated and the interference signal is achieved. The highly symmetrical arrangement can reduce the free space noise and improve the stability of the device. On the other hand, the arrangement provides integration of parallel sensing channels straightforward. Good performance was shown theoretically and experimentally. The limit of detection (LOD) for bulk sensing is 10⁻⁷ and the surface sensitivity is 0.1 pg/mm². Thus, GCI is proved to be a valuable candidate for the point of care device. RWG have proven to be a powerful tool in determine kinetics of molecular interaction and binding affinity[19]. The evanescent field in the RWGs is arising from resonant coupling of incidence via a diffraction grating. The RWG imager, recently developed imager, allows online quality control and offline data-filtering[20]. It has been reported that a LOD is down to 2.2×10⁻⁶ for bulk sensing and 0.078ng/cm² for surface sensing[20]. A growing interest in this field is to explore the activities of living cells, such as cell attachment, spreading and proliferation[21, 22]. The depth of evanescent tail limits the cell based detection since whole cells are typically 1-10µm in size. Reverse symmetry waveguide[21] with introduction of a low refractive index layer between substrate and waveguide film was demonstrated to increase the probing depth, bringing about very sensitive detection of several micrometer large bacterial or mammalian cells. Therefore, this reverse waveguide sensor with larger dynamic range can be applied to a wide range of application.

Whispering gallery mode (WGM) resonators marked with multi-analyte detection, stability in aqueous environment, low cost and footprint are increasingly being used for biosensing. For the conventional WGM resonators, however, only the evanescent tails of the resonant mode penetrate into the fluid leading to quite modest sensitivity (below 200 RUI⁻¹) [23]. To improve this scenario, hybrid plasmonic-photonics WGM resonators have come into being. Amongst those, photonic-plasmonic cavity[8,9] with extra advantages of strong energy confined in a region at nanoscale with low input power attracts attentions to the researchers. For instance, Francesco and co-workers[24] designed such device consisting of dielectric photonics crystal cavity together with a tapered silver waveguide for physical and chemical mapping. Moreover, the introduction of metallic nano-structures in close proximity to dielectric WGM resonator, shows prospects for the unprecedented sensitivity to very low concentration of target

molecules. Two main proposed configurations for bulk sensing are categorized as: microring (or micro disk) in a metal–dielectric slot configuration[25] and microring decorated with nanostripes along the circumference[26]. Another aspect, microsphere and microtoroid decorated with metallic nanoparticles such as gold nanorods, gold nano-triangle present promising performance in detecting single particle and molecule[27, 28]. However, the main challenge is the WGM damping in the metal. Consequently, the amount and distribution of nanoparticles which depend on the morphology of resonators have to be justified.

Photonic crystal-based biosensors are emerging technology which is extensively studied recently[29, 30]. A photonic crystal is a well defined nanostructure with periodically repeated variations in the refractive index. Photonic crystals contain regularly repeating regions of high and low dielectric constant and can be fabricated for one, two or three dimensions. The photonic band gap, disallowed bands of wavelengths, whose width and position are strongly dependent on the refractive index change between the dielectric materials and on the periodicity of the structure[31]. Particularly, silicon photonic crystals(PhCs) have attracted great attention owing to strong potential of integration on a chip. For instance, Dofner et al. designed and fabricated a silicon on insulator photonic crystal drop filters as refractive index sensor[32]. Two types of nanocavities either with three missing holes or a single hole are embedded between two photonic crystal waveguides so that the light is evanescently guided into cavity. The optimized Q factor is around 3000 which leads to a limit of detection of 10⁻³ RIU (Refractive Index Unit). Better performance could be obtained via optimizing the dimensions of crystal and defect and distributing the bioreceptor only in the holes.

Nano-scale optical waveguides, utilizing various nano structures, such as narrow gaps between two metallic cladding layers[33] and a triangular groove on a metal surface[34], is growingly appearing in literature. They enable lab-on-chip, monolithic integrated, miniaturized and low-cost biosensing in a simple geometry, providing a huge boost for the biosensor investigation without a bulky and complex prism-coupling architecture. In particular, slot waveguide based structures present enhanced sensitivity due to electromagnetic energy storing. Different architectures have been proposed, such as a multi-slot waveguide with metal cladding[35], and a double-slot waveguide with two metal strips located in both sides of Si nanowire[36]. Recently, we have reported a waveguide device for detecting carbohydrate-protein interaction. The performance was moderate but our train of thought was stretched on the basis of the proposed waveguide. By tuning the morphology, e.g. slots dimension and symmetry, better qualities could be achieved.

In this article, we report on the design of an integrated device and its performance in a standard immunoassay. A slot waveguide with a n-shaped gap consist of two symmetric slots embedded on opposite sides of silicon core and one slot with identical space above the silicon core. The narrower gaps with identical space of 40nm can strongly confine the field resulting in sensitivity enhancement. The symmetric geometry can simplify the manufacture as well. Combination of MZI, on the one hand, the sensitivity of integrated device is expected to be

greatly improved. A slight increase of biolayer thickness $(\delta a=0.5$ nm) might be a challenge for the pure waveguide. The detection of surface adsorbed molecule densities is down to 0.176pg/mm² for TE mode and 1.27pg/mm² for TM mode. On the other hand, the intrinsic configuration of two arms can make a parallel-control trial available. In a biochemical test, one and only one variable in a parallel-control trial is required to remove the unspecific interference from biological materials. Thus, two arms of integrated MZI should be designed morphologically identical in order to exclude the impact from configuration difference. Instead of power change detection, we take wavelength interrogation to assess antibody-antigen interaction in an immunoassay. As expected, the proposed configuration with optimum dimension presents outstanding performance. The integrated MZI not only functions as an amplifier in terms of sensitivity compared with pure slot waveguide, but also make a parallel-control trail available. All the simulation work is based on finite-element-method (FEM).

II. PROPERTY OF SLOT WAVEGUIDE

A. Schematic of slot waveguide

The cross-section view of slot waveguide with a n-shaped gap is presented in Fig.1a. The morphology of presented waveguide is symmetry compatible with simple manufacture process. The slot is 40nm in width (w_{slo}) and 40nm in height (h_{slot}) . Silicon (Si) core covered with metal cladding is the building block. The width (w_{si}) and height (h_{si}) of Si core are 350nm and 270nm. Thicknesses of silver (Ag) cladding and silica (SiO₂) buffer are setting as 3 µm. In the simulation work, the refractive indices [37] of Si and SiO₂ are 3.5046 and 1.447 respectively, at operation wavelength of 1.3µm. The wavelength selection is based on a tradeoff between the absorption loss caused by aqueous solution and the broadband light source. Water optical absorption is smaller at wavelength of 1.3µm, compared with 1.55µm wavelength common used for operation. The permittivity of silver is achieved through Durde model[38]. In Fig. 1b, the distributions of electromagnetic field of dual polarization are presented.

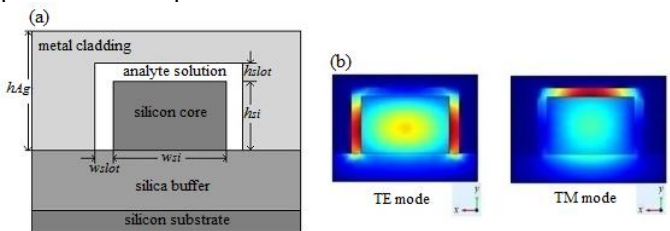


Fig. 1. (a) Cross-section view of the slot waveguide. The n-shaped slot is exposed to the analyte solution. (b) distribution of field profile in the nano-slot.

B. Characters of effective refractive index

No doubt, the effective refractive index n_{eff} is the essential physical quantity when it comes to the waveguide. The index n_{eff} depends mainly on the waveguide parameters, *i.e.* wavelength and the dimension of slots (w_{slot} and h_{slot}), bulk refractive index n_s , and biolayer thickness a. If the configuration is covered by the analyte solution, changes in effective refractive index Δn_{eff} occur when:

1. the scale of nano-slot changes.

To investigate the influence of nano-slot (w_{slot} and h_{slot}) on

effective refractive index n_{eff} , we set the w_{si} with different values (150nm, 250nm, 350nm and 450nm) and gradually increase w_{slot} from 20nm to 200nm, under the premise of the fixed $h_{si} = 320$ nm and 270nm, respectively. In Fig.2, one can see that in the case of $w_{si} > h_{si}$, for both TE and TM modes, the indices n_{eff} grow as w_{si} increasing with fixed w_{slot} . And the refractive indices n_{eff} also increase with narrower w_{slot} by w_{si} remained. when w_{slot} is large enough (normally larger than 500nm, not shown in this figure), the value of n_{eff} gradually tend to that of SOI (Si-on-insulator) waveguides without the effect of metal cladding, However, under the condition that $w_{si} < h_{si}$. only for TM mode (Fig.2b and 2d), the indices n_{eff} increase with larger w_{slot} , and gradually tend to the value of SOI waveguides. Thus, in order to get greater effective refractive index n_{eff} , the choice of $w_{si} < h_{si}$ should be avoid. From the analysis above, the waveguide with narrower slots provides stronger field confinement compared with conventional SOI waveguide, thus enhancing the interaction between the field and tested solution. However, a narrower gap induces larger propagation loss, as shown in Fig. 3. In other words, the narrower slot with stronger electromagnetic field confinement in the expense of larger loss. All in all, the trade-off between hybrid plasmonic field and propagation loss in the architecture can be selected depending on the application [39, 40].

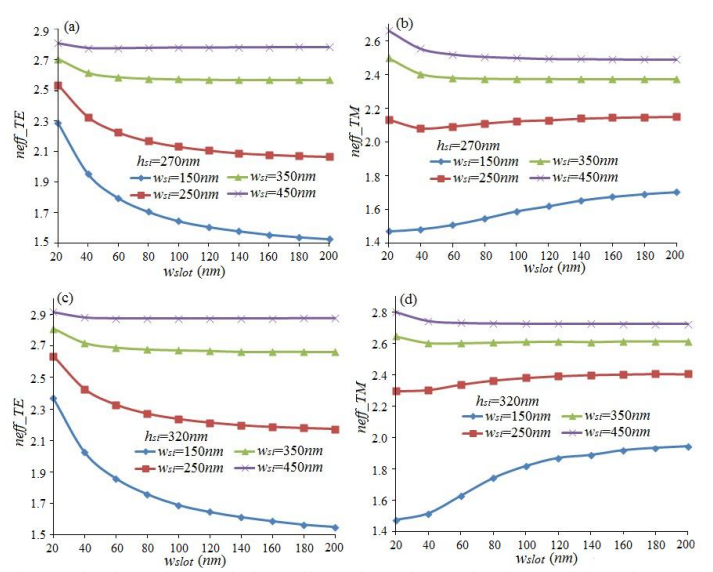


Fig. 2. The dependence of the neff on the wslot, under the condition of h_{si} = 270 nm for TE mode (a), and for TM mode(b), and the condition of h_{si} = 320 nm for TE mode (c), and for TM mode (d).

2. shifts in bulk refractive index n_s and biolayer thickness a. The influences of bulk index n_s and biolayer thickness a on effective index n_{eff} for dual polarization are sketched in Fig. 4. The effective indices (n_{eff_TE} and n_{eff_TM}) increase with biolayer thickness. Different thickness has different patterns of slope change indicating that the slot waveguide response to the different thickness with varying degrees. The slot waveguide is much more sensitive to the thickness change when the biolayer is thicker. Besides, the effective index increases with bulk index increasing. For the specific thickness, different bulk index n_s has the same effect on the effective mode index of presented configuration.

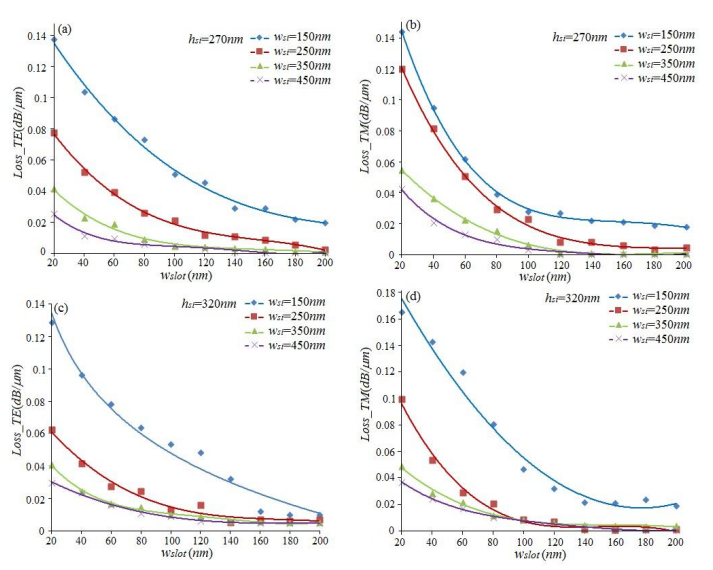


Fig. 3. The dependence of the loss on the w_{slot} , under the condition of $h_{si} = 270$ nm for TE mode (a), and for TM mode(b), and the condition of $h_{si} = 320$ nm for TE mode (c), and for TM mode (d).

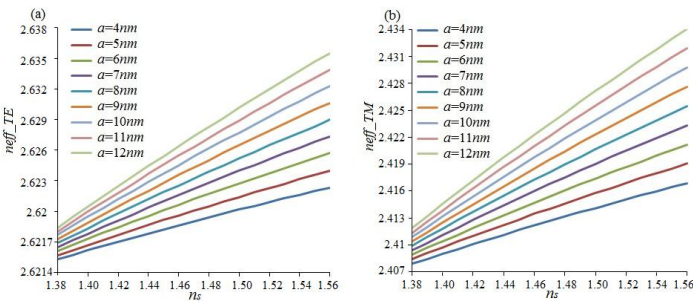


Fig. 4. The influence of n_s on effective index for TE and TM fundamental modes denoted as $n_{eff_TE}(\mathbf{a})$ and n_{eff_TM} (b) respectively, by setting layer thickness a fixed, at operating wavelength of 1.3 μ m.

C. Biochemical sensing based on slot waveguide

Herein, a standard immunoassay was emulated based on FEM. Usually, a standard immunoassay is consist of four distinct steps[5]: (1) introduction of buffer solution e.g. Phosphate Buffer Saline or PBS, (2) introducing probe molecules such as antigen or antibody to the sensor surface and forming a coating adlayer, (3) introduction of blocking solution preventing from unspecific binding, and (4) introducing target molecules (the corresponding antibody or antigen) within blocking solution to promote binding event occurring. Each step will alter the effective refractive index. For the baseline, $n_{eff TE}$ and $n_{eff TM}$ were calculated in the presence of PBS. To calculate n_{eff} TE and $n_{eff TM}$ in the presence of PBS, a variation $\delta n_s = 0.00167$ compared to water was assumed according to typical literature data[37]. We assumed[37, 41] that an uniform adlayer of 4nm thickness with $n_{film}=1.38$ for the step (2). It is supposed that introduction of blocking solution alters n_s by $\delta n_s = 0.00019$ with regard to buffer solution as well as increasing the thickness of coating adlayer by $\delta a=1$ nm. After the molecular interaction, adlayer thickness increases by $\delta a=0.5$ nm. The effective refractive indices were calculated for wavelength spanning $1.285\mu \text{m} \le \lambda \le 1.315\mu \text{m}$ at each step. The fitting curves are plotted in Fig.5. One can see clearly the process of a standard immunoassay. The effective mode index is increasing with the process of immunoassay in the range of operation wavelength.

The gaps between each curve are diverse indicating that different contributions from covering materials to the effective indices. And the result is coincident with the output spectrum in Fig.10.

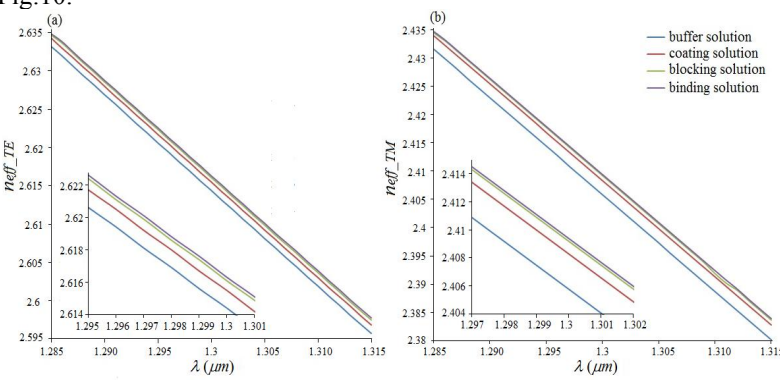


Fig. 5. Simulation results of an immunoassay at wavelength spanning 1.285 μ m $\leq \lambda \leq 1.315\mu$ m for TE mode(a) and TM mode(b) respectively. A plot of wavelength versus effective mode index provides a representation of each step.

Afterwards, the spectral interrogation sensitivity, caused by changes Δn_s can be defined as follows:

$$S_{WG_n_i} = \frac{\partial \lambda}{\partial n_s} = \frac{\partial \lambda}{\partial n_{eff_i}} \cdot \frac{\partial n_{eff_i}}{\partial n_s} \quad (i = TE, TM)$$
 (1)

where the terms $\partial \lambda / \partial n_{eff_i}$ and $\partial n_{eff_i} / \partial n_s$ can be obtained from Fig.5 and Fig.4, respectively. The data of $S_{WG_n_i}$ is plotted in Fig.6a and 6b.

Similarly, the spectral interrogation sensitivity, caused by changes Δa , can be defined as follows:

$$S_{WG_a_i} = \frac{\partial \lambda}{\partial a} = \frac{\partial \lambda}{\partial n_{eff_i}} \cdot \frac{\partial n_{eff_i}}{\partial a} \ (i = TE, TM)$$
 (2)

where the value of $\partial n_{eff_{-}}/\partial a$ can be also achieved by Fig.4. The results are shown in Fig.6d and 6c.

Bulk index n_s has greater influence on spectral interrogation sensitivity, compared to the weak effect of biolayer thickness a which has a horizontal fitting curve without a slope. Thus, to maximum the sensitivity, MZI configuration is adopted due to its sensitive to small change of ambient medium.

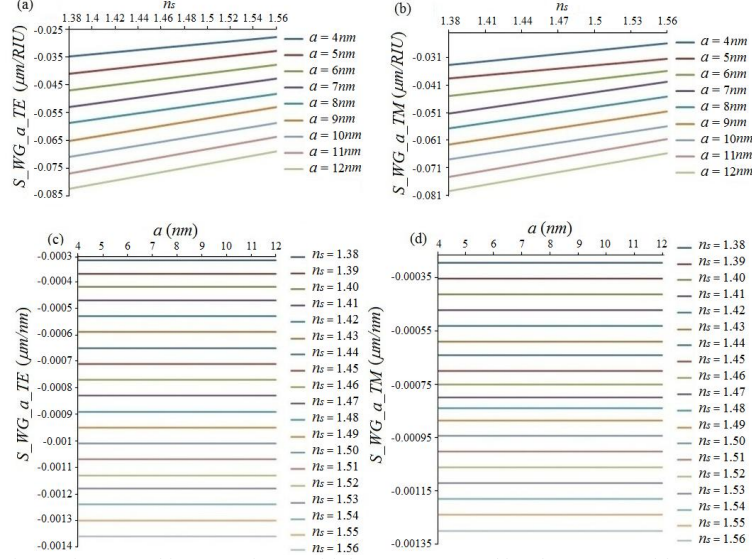


Fig. 6. The spectral interrogation sensitivity $S_{WG_{n-1}}$, caused by changes Δn_s with different adlayer thickness (4nm-12nm) at $\lambda = 1.3 \mu$ m, where (a) is for TE polarization, and (b) for TM polarization. The dependence of spectral

interrogation sensitivity $S_{WG_{_a,i}}$ on adlayer thickness a with fixed n_s ranging from 1.38 to 1.56, is presented, at λ =1.3 μ m, where (c) is for TE polarization, and (d) for TM polarization.

III. PROPERTY OF INTEGRATED OPTICS

A. Architecture of integrated optics

The model of integrated optics is sketched in Fig.7. The dimension of the device is $160\mu m$ in length (L). Sensing and reference arms have identical length L_m =60 μ m and been separated by the distance $D=21\,\mu\text{m}$. The Y-splitter is composed of S-shaped bent wires with bending radius of 25 μ m $(r_0=25 \,\mathrm{\mu m})$. The length of slot waveguide l, is 10 $\,\mathrm{\mu m}$ with a width of $6.5 \mu m$ ($w=6.5 \mu m$). Cytop material [42] with refractive index very similar to pure water is adopted to cover the proposed structure so as to prevent the external disturbance. The geometric configuration of both arms is identical so that a parallel-control trial can be carried on. Instead of adding target molecules in the last step, PBS buffer is flowed over the reference area. In this way, we can exclude the background from biological materials throughout the immunoassay, including buffer molecules, probe molecules and blocking molecules. All the biological materials with optical parameters added in both arms of integrated MZI were shown in table 1.

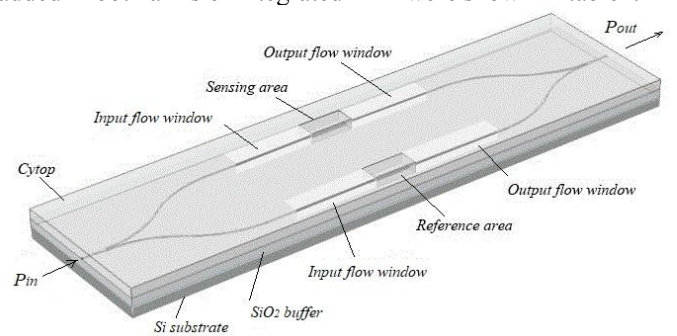


Fig. 7. 3D schematic structure of integrated optics with morphologically identical arms.

Table 1. Biological materials flowed over the integrated MZI in a standard immunoassay.

minutioussuj.						
	sensing area			reference area		
material	bulk	adlayer	adlayer	bulk	adlayer	adlayer
	index	index	thickness	index	index	thickness
PBS	1.33167	0	0	1.33167	0	0
buffer						
coating	1.33167	1.38	4	1.33167	1.38	4
solution	1.55107	1.50		1.55107	1.50	
blocking	1.33186	1.38	5	1.33186	1.38	5
solution	1.33100	1.30	J	1.33100	1.30	<u> </u>
target	1.33186	1.38	5.5	1.33186	1.38	5.5
solution	1.55100	1.50	5.5	1.55160	1.50	5.5

B. Spectral interrogation sensitivity

Spectral interrogation sensitivity S_{MZI} either caused by bulk index or thickness was defined and subsequently taken to evaluate the performance of the device. For a typical MZI the phase difference $\Delta\Phi$ is generally expressed as[5]:

phase difference
$$\Delta\Phi$$
 is generally expressed as[5]:

$$\Delta\Phi = \frac{2\pi L_m}{\lambda} \left(n_{eff_s_i} - n_{eff_r_i} \right) \quad (i = TE, TM)$$
(3)

where λ is the operating wavelength, $n_{eff_s_i}$ and $n_{eff_r_i}$ denoting effective refractive indices of the sensing and reference arms

respectively.

For Eq.3, keeping $\Delta\Phi$ as constant and taking partial differentiation with respect to λ , we can get the expression:

$$\frac{\partial}{\partial \lambda} \left[\frac{1}{\lambda} \left(n_{eff_s_i} - n_{eff_r_i} \right) \right] = 0 \quad (i = TE, TM)$$
(4)

and works out to:

so out to:

$$\lambda \cdot \frac{\partial (n_{\text{eff}_s_i} - n_{\text{eff}_r_i})}{\partial \lambda} = n_{\text{eff}_s_i} - n_{\text{eff}_r_i} \quad (i = TE, TM) \quad (5)$$

By introducing ∂n_s to the left-hand side of Eq.5, we can rewrite the above as:

$$\lambda \cdot \frac{\partial \left(n_{eff_s_i} - n_{eff_r_i}\right)}{\partial n_s} \cdot \frac{\partial n_s}{\partial \lambda} = n_{eff_s_i} - n_{eff_r_i} \ (i = TE, TM) \ (6)$$

Finally defining

$$S_{MZI_{_n_i}} = \frac{\partial \lambda}{\partial n_s} \bigg|_{a=const} = \frac{\lambda}{n_{eff_s_i} - n_{eff_r_i}} \frac{\partial \left(n_{eff_s_i} - n_{eff_r_i}\right)}{n_{eff_s_i} - n_{eff_r_i}}$$
 (*i* = TE, TM) (7)

where $S_{MZI_n_i}$ is the spectral interrogation sensitivity caused by bulk index over the sensing area, with adlayer thickness remained. The term $\partial(n_{eff_s_i} - n_{eff_r_i})/\partial n_s$ is changes $\partial(n_{eff_s_i} - n_{eff_r_i})$ produced by the shift ∂n_s , at operating wavelength λ . The result was calculated and sketched in Fig. 8. The proposed device is more sensitive to the shift in bulk index with small value for a fixed biolayer thickness, according to the gradient of fitting curve. Likewise, we can derive the spectral interrogation sensitivity caused by adlayer thickness over the sensing area, with n_s fixed:

$$S_{MZI_a_i} = \frac{\partial \lambda}{\partial a}\bigg|_{n_s = const} = \frac{\lambda}{n_{eff_s_i} - n_{eff_r_i}} \frac{\partial \left(n_{eff_s_i} - n_{eff_r_i}\right)}{\partial a}\bigg|_{n_s = const}$$

$$(i = TE, TM)$$
(8)

The result was computed and plotted in Fig. 9. As expected, the spectral interrogation sensitivity to the thickness change is largely enhanced, compared to the slot waveguide.

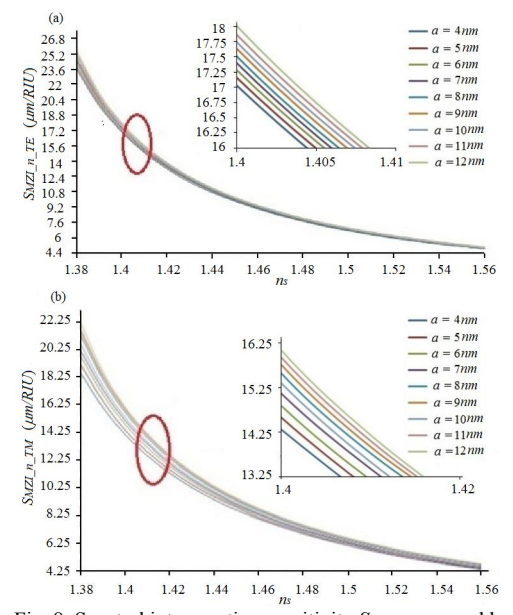


Fig. 8. Spectral interrogation sensitivity $S_{MZI_{-n.i}}$ caused by n_s with a fixed, at 1.3 μ m operation wavelength, where (a) is for TE mode and (b) for TM mode.

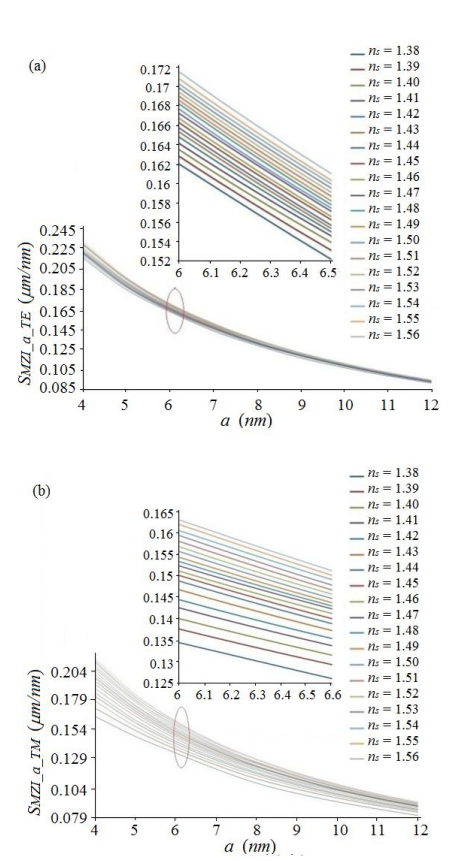


Fig. 9. The dependence of $S_{MZI_n.i}$ on n_s with a fixed, at 1.3 μ m operation wavelength, where (a) is for TE mode and (b) is for TM mode.

The integrated optics shows enhanced sensitivity with three orders of magnitude compared to simple slot waveguide, according to Fig. 6 and Fig. 8-9. The term $S_{MZI,n,i}$ can reach as high value as 25800nm/RIU for TE polarization and 22213nm/RIU for TM, compared with 83nm/RIU for TE mode and 73nm/RIU for TM mode obtained from slot waveguide. And $S_{MZI\ a\ i}$ can arrive 230nm/nm for TE mode and 215nm/nm for TM mode, compared to 1.3nm/nm for TE polarization and 1.28nm/nm for TM polarization with waveguide only. With the spectral sensitivity, the detectable minimum value of Δn_s are 3.88×10⁻⁶ RIU for TE mode and 4.5×10⁻⁶RIU for TM mode and that of Δa are 4.34×10^{-4} nm for TE mode and 4.6×10^{-3} nm for TM mode. Thus, the minimum detectable signal response Δn_{eff} can be achieved ($\Delta n_{eff_TE} = 2.67 \times 10^{-7}$ and $\Delta n_{eff_TM} = 33.55 \times 10^{-7}$). It is corresponding to the mass coverage[43] of 0.176pg/mm² for TE mode and 1.27pg/mm² for TM mode.

The output spectrums of a standard immunoassay are shown schematically in Fig.10. Resonance wavelength λ_{res} increases with the refractive indices of the covering solution (from coating solution to target molecule solution). With the process of immunoassay, the indices of the elements in the sensing arm will increase more than those in the reference arm, resulting in red shift of wavelength. Moreover, numerical value of red-shifted wavelength λ_{res} varies due to different influence on the effective mode index over sensing arm of covering materials, which is also in agreement with the results in Fig.5. For instance, λ_{res} caused by coating solution is red shifted 4nm, while the resonant wavelengths induced by blocking solution and target molecules are red shifted 6nm and 7nm respectively, for TM polarization.

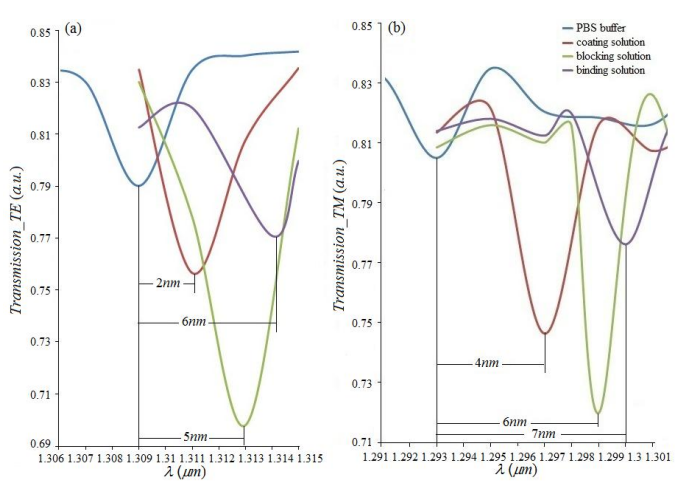


Fig. 10. The dependence of resonance wavelength on transmissions in the MZI sensor. The reference level is the transmission response of PBS buffer. The red and green lines are measured results when the sensing area is covered with coating solution and blocking solution. And the purple line is the measured results when target molecules are introduced to the sensing arm. (a) for TE mode and (b) for TM mode.

Last but not least, we have envisaged a CMOS-compatible fabrication process of the designed device. The process can start from a commercial SOI wafer. Alternatively the plasma enhanced chemical vapor deposition (PECVD) technology is used to deposit the SiO₂ and alpha-Si thin film on Si substrate. The photoresist thin film is formed on Si film and the waveguide patterns are constructed using an E-beam lithography so as to gaining high resolution. Then an extreme thin aluminum (Al) film with 40nm is deposited on the sidewall and top of the Si rib by sputtering process. This step could be followed by the deposition of an Ag layer with 3µm thickness on the sidewall and the top of the Al film by sputtering process. Afterwards, the Al film is removed by selectively etched to form the n-shaped slot. The patterned configuration is constructed in both sensing and reference arms of MZI. Cytop layer is employed to cover the designed structure so as to avoid external interference. Finally, the sensor is coupled to microfluidic module in two arms, which allows for sample introduction and real-time monitoring.

IV. CONCLUSION

In this paper, we have theoretically designed the integrated MZI biosensor for a standard immunoassay. A parallel-control trial is carefully designed so that the interference from biological materials throughout the immunoassay can be removed. The spectral interrogation sensitivities of the integrated optics, caused by bulk index and adlayer thickness, are derived mathematically to evaluate the quality of biosensor. The corresponding mass coverage is down to 0.176pg/mm² for TE mode and 1.27pg/mm² for TM mode. Numerical analysis shows that sensitivity of the integrated sensor is three orders of magnitude larger than that of simple slot waveguide. Hence, coupling the waveguide to MZI can significantly promote the sensitivity in the detection. The resonance wavelengths shift to the right (longer wavelengths) with different numerical values, when infiltrated with higher refractive index solution. The novel device could be achieved by a simple and

CMOS-compatible fabrication process. The novel structure proposed with the help of numerical and simulation analysis lays a good basis for the follow up work. The proposed device used in biochemical sensing experimentally has been planed to carry out.

ACKNOWLEDGMENT

The authors gratefully acknowledge the financial support for this work provided by the National Natural Science Foundation of China (NSFC) under Grant Nos. 61235003 and 61427816. This work was also supported by the Collaborative Innovation Center of Suzhou Nano Science and Technology.

REFERENCE

- 1. SD Gan and KR Patel, "Enzyme Immunoassay and Enzyme-Linked Immunosorbent Assay," *J Invest. Dermatol.*, vol. 133, no. 9, pp. 1-3, Sep. 2013. 2. DK Chatterjee, K Sitaraman, C Baptista, J Hartley, TM Hill and DJ Munroe, "Protein Microarray On-Demand: A Novel Protein Microarray System," *PLoS One*, vol. 3, no. 9, pp. e3265, Sep. 2008.
- 3. AE Bolton and WM Hunter, "The labelling of proteins to high specific radioactivities by conjugation to a ¹²⁵I-containing acylating agent. Application to the radioimmunoassay," *Biochem J.*, vol. 133, no. 9, pp. 529-539, Jul. 1973. 4. F Prieto, B Sepulveda, A Calle, A Llobera, C Dominguez, A Abad, A Montova and LM Lechuga, "An integrated optical interferometric nanodevice based on silicon technology for biosensor applications," *Nanotechnol.* vol. 14, no. 8, pp. 578-584, Jul. 2003.
- 5. M Kitsara, K Misiakos, I Raptis and E Makarona, "Integrated optical frequency-resolved Mach-Zehnder interferometers for label-free affinity sensing," *Opt. Express*, vol. 18, no. 8, pp. 8193-8206, Apr.2010.
- BJ Luff, JS Wilkinson, J Piehler, U Hollenbach, "Integrated Optical Mach–Zehnder Biosensor," J Lightwave Technol., vol.16, no. 4, pp. 583-592 Apr. 1998.
- 7. F. Prieto, B Sepulveda, A Calle, A Llobera, C Dominguez, LM Lechuga, "Integrated mach-Zehnder interferometer based on ARROW structures for biosensor applications," *Sens. Act. B*, vol. 92, no. 1-2, pp. 151-158, Jul. 2003.
- 8. WC Tsai and IC Li, "SPR-based immunosensor for determining staphylococcal enterotoxin A," *Sens. Act. B*, vol. 136, no. 1, pp. 8-12, Feb. 2009.
- 9. Al Lao, X Su and KM Aung, "SPR study of DNA hybridization with DNA and PNA probes under stringent conditions," *Biosens. Bioelectron*, vol. 24, no. 6, pp. 1717-1722, Feb. 2009.
- 10. C Chen, X Hou and J Si, "Protein analysis by Mach-Zehnder interferometers with a hybrid plasmonic waveguide with nano-slots," *Opt. Express*, vol. 25, no. 25, pp. 31294-31308, Dec. 2017.
- 11. L Xu, VG Vaidyanathan and BP Cho, "Real-time surface plasmon resonance study of biomolecular interactions between polymerase and bulky mutagenic DNA lesions," *Chem Res Toxicol*, vol. 27, no. 10, pp. 1796-1807, Sep. 2014.
- 12. RC Jorgenson and SS Yee, "A fiber-optic chemical sensor based on surface plasmon resonance," *Sens. Act. B*, vol. 12, no. 3, pp.213-218, Apr. 1993.
- 13. AW Sonesson, TH Callisen, H Brismar and UM Elofsson, "A comparison between dual polarization interferometry (DPI) and surface plasmon resonance (SPR) for protein adsorption studies," *Colloid Surface B*, vol. 54, no. 2, pp. 236-240, Feb. 2007.
- 14. I Raptis, E Makarona, P Petrou, SE Kakabakos and K Misiakos, "Monolithic optoelectronic chip for label-free multi-analyte sensing Applications," *Proc. of SPIE*, vol. 8976, pp. 89760X, Mar. 2014.
- 15. M.-C. Estevez, M Alvarez amd LM Lechuga, "Integrated optical devices for lab-on-a-chip biosensing applications," *Laser Photonics Rev.*, vol. 6, no. 4, pp. 463-487, Jul. 2012.
- 16. P Kozma, A Hamori, K Cottier, S Kurunczi and R Horvath, "Grating coupled interferometry for optical sensing," *Appl. Phys. B.*, vol. 97, no.1, pp. 5–8. Sep. 2009.
- 17. P Kozma, A Hamori, S Kurunczi, K Cottier and R Horvath, "Grating coupled optical waveguide interferometer for label-free biosensing," *Sens. Actuators B Chem.*, vol. 155, no. 2, pp. 446–450, Jul. 2011.
- 18. D Patko, K Cottier, A Hamori and R Horvath, "Single beam grating coupled interferometry: high resolution miniaturized label-free sensor for plate based parallel screening" *Opt Express.*, vol. 20, no. 21, pp. 23162-23173, Oct. 2012.

- 19. Y Fang, AM Ferrie, NH Fontaine, J Mauro and J Balakrishnan, "Resonant Waveguide Grating Biosensor for Living Cell Sensing," *Biophys J.*, vol. 91, no. 5, pp.1925-1940, sep. 2006.
- 20. N Orgovan, B Kovacs, E Farkas, B Szabó, N Zaytseva, Y Fang and R Horvath, "Bulk and surface sensitivity of a resonant waveguide grating imager," *Appl. Phys. Lett.*, vol. 104, no. 8, pp. 083506, Feb. 2014.
- 21. R Horvath, HC Pedersen, N Skivesen, D Selmeczi and NB Larsen, "Monitoring of living cell attachment and spreading using reverse symmetry waveguide sensing," *Appl. Phys. Lett.*, vol. 86, no. 7, pp. 071101, Feb. 2005.
- 22. N Orgovan, B Peter, S Bősze, JJ Ramsden, B Szabó and R Horvath, "Dependence of cancer cell adhesion kinetics on integrin ligand surface density measured by a high-throughput label-free resonant waveguide grating biosensor," *Sci Rep.*, vol. 4, pp. 4034, Feb. 2014.
- 23. Bozzola A, Perotto S and De Angelis F, "Hybrid plasmonic-photonic whispering gallery mode resonators for sensing: a critical review," Analyst, vol. 142, no. 6, pp. 883-898, Feb. 2017.
- 24. AF De, G Das, P Candeloro, M Patrini, M Galli, A Bek, M Lazzarino, I Maksymov, C Liberale, LC Andreani and FE Di, "Nanoscale chemical mapping using three-dimensional adiabatic compression of surface plasmon polaritons," *Nat. Nanotechnol.*, vol. 5, no. 1, pp. 67–72, Jan. 2010.
- 25. MS. Kwon, B Ku and Y Kim, "Plasmofluidic Disk Resonators," *Sci. Rep.*, vol. 6, pp. 23149, Mar. 2016.
- 26. M Zhang, B Liu, G Wu and D Chen, "Hybrid plasmonic microcavity with an air-filled gap for sensing applications," *Opt Commun.*, vol. 380, pp.6-9,Dec. 2016.
- 27_20. MD Baaske, MR Foreman and F Vollmer, "Single-molecule nucleic acid interactions monitored on a label-free microcavity biosensor platform," *Nat. Nanotechnol.*, vol. 9, no. 11, pp. 933–939, Nov. 2014.
- 28. E Arbabi, SM Kamali, S Arnold and LL Goddard, "Hybrid whispering gallery mode/plasmonic chain ring resonators for biosensing," *Appl. Phys. Lett.*, Vol. 105, no. 23, pp. 231170, Dec. 2014.
- 29. RV Nair and R Vijaya, "Photonic crystal sensors: an overview," *Prog. Quantum Electron.*, vol. 34, no. 3, pp. 89-134, May 2010.
- 30. JD Joannopoulos, SG Johnson, JN Winn and RD Meade. Photonic Crystals. Moding the Flow of Light. (Princeton University Press, 2008).
- 31. ID Block, N Ganesh, M Lu and BT Cunningham, "A Sensitivity Model for Predicting Photonic Crystal Biosensor Performance," IEEE Sens. J., vol. 8, no. 3, pp. 274-280, Mar. 2008.
- 32. DF Dorfner, T Hurlimann, T Zabel, LH Frandsen, G Abstreiter and JJ Finley, "Silicon photonic crystal nanostructures for refractive index sensing," *Appl. Phys. Lett.*, vol. 93, pp. 181103, Nov. 2008.
- 33. R Zia, MD Selker, PB Catrysse, ML Brongersma, "Geometries and materials for subwavelength surface plasmon modes," *J. Opt. Soc. Am. A*, vol. 21, no. 12, pp. 2442–2446, Dec. 2004.
- 34. DF Pile, and DK Gramotnev, "Channel plasmon-polariton in a triangular groove on a metal surface," *Opt. Lett.*, vol. 29, no. 10, pp. 1069–1071, May 2004
- 35. C Chen, X Hou and J Si., "Carbonhydrate-protein interactions characterized by dual polarization hybrid plasmonic waveguide," *Nanotechnol Rev.*, vol. 1, no.1, pp. 11-18, Feb. 2018.
- 36. X Sun, D Dai, L Thylen, L Wosinski, "High-sensitivity liquid refractive-index sensor based on a Mach-Zehnder interferometer with a double-slot hybrid plasmonic waveguide," *Opt. Express*, vol. 23, no. 20, pp.25688-25699, Oct. 2015.
- 37. Lide and David R. CRC Handbook of Chemistry and Physics, Internet Version (Taylor and Francis, Boca Raton, FL, 2007)
- 38. CF Bohren and DR Huffman. Absorption and Scattering of Light by Small Particle (John Wiley &Sons, Inc., 1983)
- 39. RF Oulton, VJ Sorger, DA Genov, DFP Pile and X Zhang, "A hybrid plasmonic waveguide for subwavelength confinement and long-range propagation," *Nat. Photonics*, vol. 2, no. 8, pp. 496-500, Jul. 2008.
- 40. D Dai, Y Shi, S He, L Wosinski and L Thylen, "Silicon hybrid plasmonic submicron-donut resonator with pure dielectric access waveguides," Opt. Express, vol. 19, no. 24, pp. 23671-23682, Nov. 2011.
- 41. J. Voros, "The density and refractive index of Adsorbing Protein Layers," Biophys. J., vol. 87, no. 1, pp. 553–561, Jul. 2004.
- 42. http://www.bellexinternational.com/products/cytop/
- 43. J. A. De Feijter, J. Benjamins, and F. A. Veer, "Ellipsometry as a tool to study the adsorption behavior of synthetic and biopolymers at the air-water interface," *Biopolymers*, vol. 17, no. 7, pp. 1759–1772, Jul. 1978.